CrossMark

TOPICAL COLLECTION: INTERNATIONAL CONFERENCE ON THERMOELECTRICS 2017

Preparation and Thermoelectric Properties of Graphite/Bi$_{0.5}$Sb$_{1.5}$Te$_3$ Composites

WENHUA HU,[1] HONGYU ZHOU,[1] XIN MU,[1] DANQI HE,[1] PENGXIA JI,[1] WEIKANG HOU,[1] PING WEI,[1,2] WANTING ZHU,[1] XIAOLEI NIE,[1] and WENYU ZHAO[1,3]

1.—State Key Laboratory of Advanced Technology for Materials Synthesis and Processing, Wuhan University of Technology, Wuhan 430070, China. 2.—e-mail: pingwei@whut.edu.cn. 3.—e-mail: wyzhao@whut.edu.cn

Bismuth telluride zone-melting alloys are the most commercially used thermoelectric materials. However, the zone-melting ingots have weak machinability due to the strong preferred orientation. Here, non-textured graphite/Bi$_{0.5}$Sb$_{1.5}$Te$_3$ (G/BST) composites were prepared by a powder metallurgy method combined with cold-pressing and annealing treatments. The composition, microstructure, and thermoelectric properties of the G/BST composites with different mass percentages of G were investigated. It was found that G addition could effectively reduce the thermal conductivity and slightly improve the electrical properties of the BST, which resulted in a large enhancement in the figure-of-merit, ZT. The largest ZT for the xG/BST composites with $x = 0.05\%$ reached 1.05 at 320 K, which is increased by 35% as compared with that of the G-free BST materials. This work provided an effective method for preparing non-textured Bi$_2$Te$_3$-based TE materials with a simple process, low cost, and large potential in scale production.

Key words: Bi$_{0.5}$Sb$_{1.5}$Te$_3$, graphite, composite thermoelectric materials, thermoelectric properties

INTRODUCTION

Thermoelectric (TE) materials, which can realize direct energy conversion between electricity and heat, have attracted great attention in the applications of power generation and solid-state cooling.[1–3] The conversion efficiency of a TE material depends on the dimensionless figure-of-merit, $ZT = \alpha^2 \sigma T / \kappa$, where σ is the electrical conductivity, α is the Seebeck coefficient, T is the absolute temperature, and κ is the thermal conductivity ($\kappa = \kappa_E + \kappa_L$, where κ_E is the electronic contribution and κ_L is the lattice contribution). A high-ZT TE material should be a perfect combination of a large power factor ($\alpha^2 \sigma$) and a low κ. Two kinds of approaches have been proposed for developing high-performance TE materials. One is to exploit new material families that possess superior properties, such as cage-like filled skutterudites and several layered compounds,[4–10] while another is to optimize the transport properties of the traditional TE materials, such as PbTe and Bi$_2$Te$_3$ alloys, by means of band engineering[11] or nanostructure engineering.[12–15]

Up to now, traditional Bi$_2$Te$_3$-based alloys still rank as the most successful commercialized TE materials that are widely used in the working temperature range of 300–500 K.[1] Commercialized zone-melting Bi$_2$Te$_3$-based ingots usually have $ZT \sim 1.0$ for p-type and ~ 0.8 for n-type materials. However, the zone-melting ingots present strong anisotropic properties and weak machinability because of their van der Waals layered structure, which restricts wider applications.[16,17] It is thus necessary to fabricate Bi$_2$Te$_3$-based materials with less preferred orientations in microstructure and enhanced isotropic TE performance. In recent decades, nanostructuring engineering has provided

a powerful tool for preparing less-textured Bi$_2$Te$_3$-based materials with nanosized grains and improved TE performance.[14,16,17] However, the preparation of this kind of material still requires more low-cost and mass-productive methods.

In this work, a traditional powder metallurgy method was used to pulverize the commercialized zone-melting p-type Bi$_{0.5}$Sb$_{1.5}$Te$_3$ (BST) ingots, and then the pulverized powders were quickly cold-pressed and annealed to obtain BST pellets. Since the commonly used hot-pressing treatment was avoided, the annealed cold-pressed pellets showed no signature of preferred orientation, and, moreover, this preparation method was much simpler and less costly. In order to further optimize the TE properties of the cold-pressed pellets, graphite (G) micro-particles were added as the secondary phase. In fact, carbon materials, especially carbon nanotubes and graphene-related materials,[18–25] have been used as important additions to enhance the performance of TE materials. Here, the use of G particles also has the advantages of low cost and easy control. The effects of G particles on the phase composition, microstructure, and TE properties of xG/BST (x = 0%, 0.05%, 0.10%, 0.15%, and 0.20%) composite TE materials were investigated. It was revealed that optimizing the content of G particles could effectively reduce the κ of the p-type BST material without a significant influence on the power factor, which resulted in enhancements in ZT. The largest ZT value reached 1.05 at 320 K for the composite with x = 0.05%, which is increased by 35% as compared with that of G-free BST materials.

EXPERIMENTAL

The preparation procedure of xG/BST composite TE materials was implemented as follows. Firstly, the starting materials were commercialized zone-melting BST ingots. After being crushed, the ingots were pulverized with a planetary ball mill apparatus at a speed of 200 rpm for 4 h under the protection of argon. The yielded powder had the particle size of 1–5 μm. Secondly, G particles, BST powder, and alcohol solvent was loaded into a beaker, then ultrasonically dispersed for 10 min at room temperature to form G/BST powders. The added contents of G particles for each xG/BST (x = 0–0.20% in weight) composites were calculated according to the mass of the ball-milled BST powder (1.5 g). The size of the G particles is less than 5 μm and the average size is about 1 μm. Thirdly, after drying, the as-prepared composite powders were cold-pressed under a pressure of 20 MPa. The cold-pressed cylinders were 15 mm in diameter and about 1.5 mm in height. Finally, the cylinders were annealed in a horizontal tube furnace at 673 K for 2 h in a flowing hydrogen atmosphere.

The constituent phases of all the composites were determined by x-ray diffraction (XRD; PANalytical X'Pert Pro) using Cu Kα radiation (λ = 0.15418 nm).

The microstructures of the G and the samples were analyzed by the scanning electron microscopy (Zeiss ULTRA-PLUS-43-13). The chemical compositions and microstructures of all the composites were analyzed by electron probe microanalysis (JXA-8230). The Hall coefficient (R_H) was measured at room temperature by the van der Pauw method using a thermoelectric and magnetic performance testing system (NYMS-1). Meanwhile, α and σ were measured using the standard four-probe method by NYMS-1. All the electrical properties (R_H, α and σ) were tested perpendicular to the cold-press direction. The carrier concentration (n) and mobility (μ) were calculated using the formula $n = 1/(R_H e)$ and $\mu = R_H/\rho$, and κ was calculated by using the equation $\kappa = \lambda \rho C_p$, where C_p is the specific heat capacity, ρ is the density of materials, and λ is the thermal diffusivity coefficient. λ was measured by the laser-flash technique (Netzsch LFA-427) in a flowing argon atmosphere. C_p was measured using a Q20 differential scanning calorimeter. Thermal properties (λ) were measured along the cold-press direction. ρ was obtained by the Archimedes method. κ_L was obtained by subtracting κ_E from κ using the equation $\kappa_L = \kappa - \kappa_E$. Here, κ_E was calculated by the Wiedemann–Franz law $\kappa_E = \sigma L T$, where L is the Lorenz number, $L = 2.0 \times 10^{-8}$ V^2 K^{-2}. σ, α, and κ were measured in the temperature range from 300 K to 480 K. Uncertainties for σ and α were $\pm$ 5–7% and for κ was $\pm$ 10%.

RESULTS AND DISCUSSION

Figure 1 shows the XRD patterns of the surfaces of the xG/BST bulk samples. All the diffraction peaks can be indexed to the standard pattern of BST (JCPDS 49-1713). The characteristic diffraction peaks assigned to G were not detected in the composites as the content of G varied from 0.05% to 0.20%. This was understandable since the content of G was much lower than the XRD detection (around 1%). Compared to the standard XRD pattern, the measured patterns did not show obvious preferential orientations. Since the commonly used hot-pressed treatment was avoided, the realignment of BST grains at high temperature should be largely suppressed, which resulted in a non-textured microstructure.

Figure 2 shows the backscattered electron image (BEI) and the secondary electron image (SEI) of BST (a, b) and 0.05%G/BST composites (c, d). Since we used a cold-pressing process for sample densification, many pores can be found in the samples. The pore size of the BST is mostly around several micrometres, and for the 0.05%G/BST composites it is smaller (1–5 μm). After adding G into the BST matrix, more pores can be found in the G/BST composites. The formation of pores in the composites should be caused by the cold-pressing process, which led to a low density, as listed in Table I. The density decreased as the G content x increased due

to the increased pores and also the low density of G. Figure 3 shows the SEI (a), BEI (b), and the elemental mapping images of the 0.05% G/BST composites. The mapping images showed the existence of G and the uniformly distributed matrix elements (Bi, Sb, and Te). The oxidation of G could be minimized since the samples were annealed in a flowing hydrogen atmosphere.

The room-temperature charge transport properties of the xG/BST composites are listed in Table I. The positive Hall coefficient values indicated that the majority carriers of the composites were holes, indicative of a p-type conduction behavior. The $R_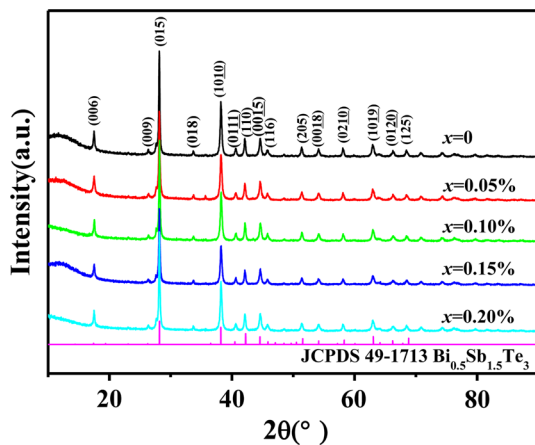H$ and μ of xG/BST composites first increased and then decreased as x was increased. Meanwhile, the n first decreased and then increased. The composites with $x = 0.05\%$ and $x = 0.10\%$ exhibited increments in the R_h and μ as well as decreases in the n as compared with the G-free sample. The decrease of n should be attributed to the decreased density, while the increased μ was a consequence of improved electrical transport contributed by the G. The composites with $x = 0.15\%$ and $x = 0.20\%$ exhibited a decrease in μ as well as an increase in n as compared with the composites with $x = 0.10\%$. A possible explanation for this change is that the carrier number provided by the G particles increased with increasing their content, which led to increased n and thus decreased μ. Therefore, the addition of a proper amount of G can be used to regulate the carrier transport of the BST matrix.

The temperature dependences of electrical conductivity, Seebeck coefficient, and power factor in the range of 300–480 K of xG/BST composites are shown in Fig. 4. The decrease of σ with increasing the measuring temperature suggested a metal-like conduction behavior. The low σ should be strongly relevant to the low density of the samples as determined by the preparation methods. With increasing x, the σ of xG/BST composites first decreased and then significantly increased for the $x = 0.20\%$ composite. This was attributed to the competition on the change in n and μ according to the formula $\sigma = ne\mu$. With increasing the G content x, the carrier concentration of xG/BST composites decreased for the samples with $x \leq 0.10\%$ and then increased for those with $x > 0.10\%$. The decreased n for the samples with $x \leq 0.10\%$ should be attributed
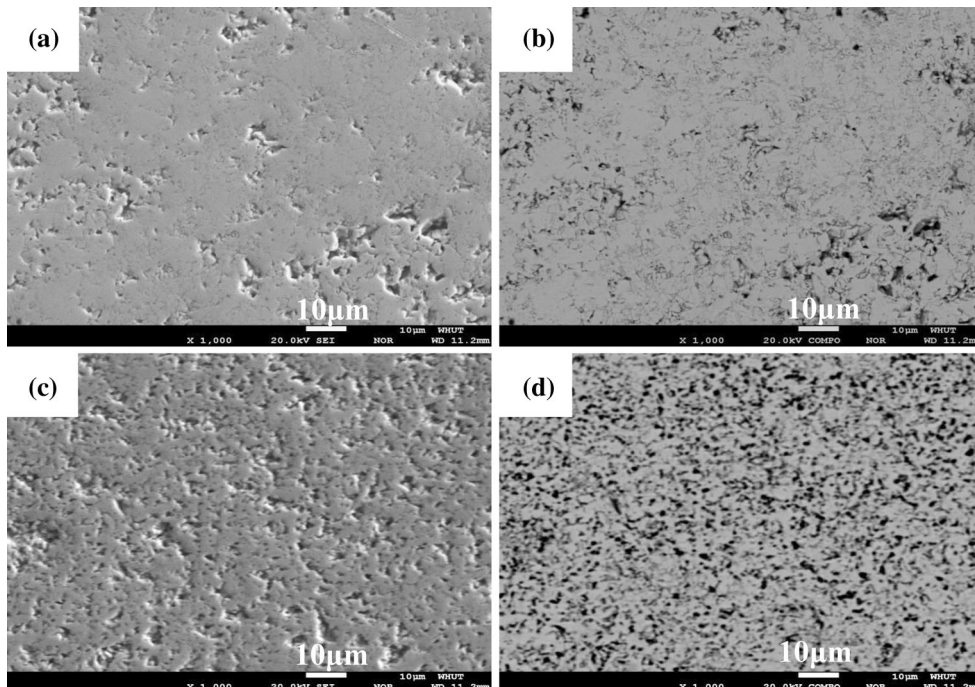

Fig. 1. XRD patterns of xG/BST composites.

Fig. 2. SEI and BEI of BST (a, b) and 0.05%G/BST composites (c, d).

Table I. Density and charge transport properties of xG/BST composites at room temperature

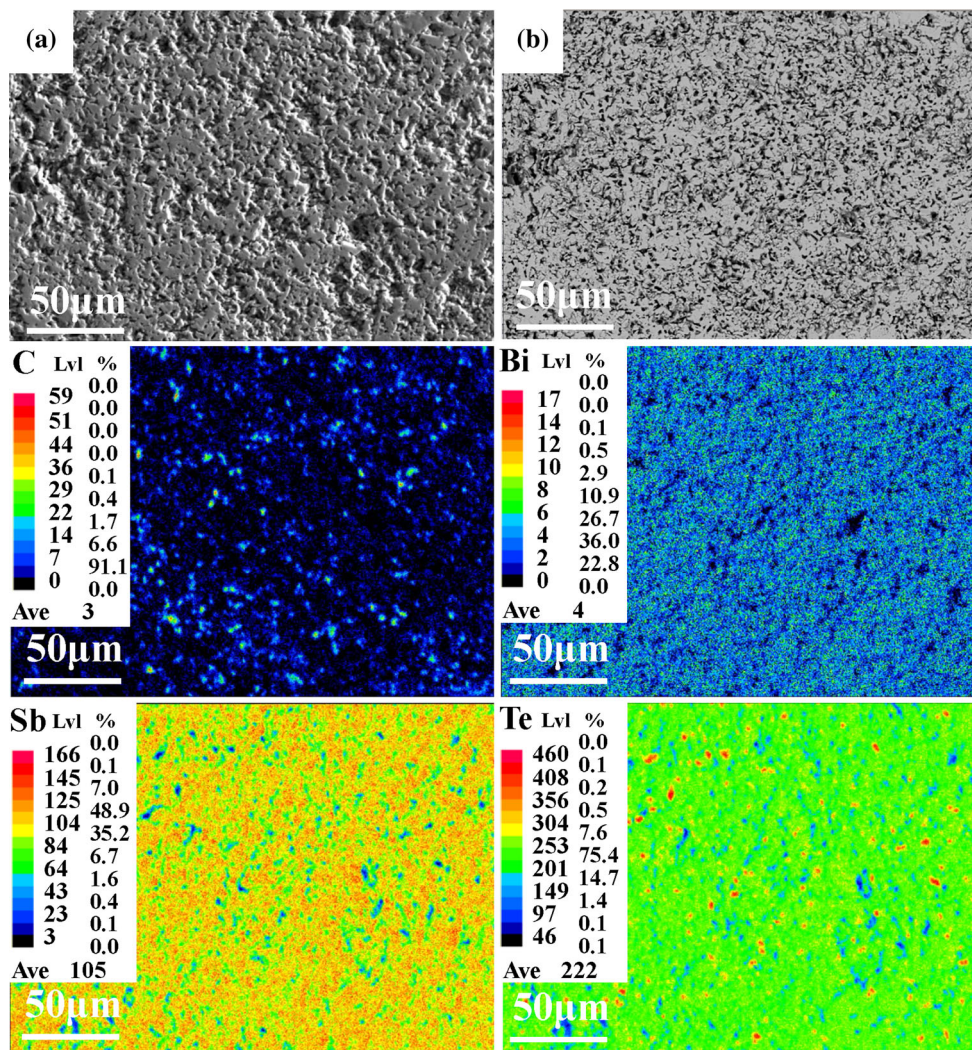| Sample	Density (g cm^{-3})	Hall coefficient (cm^3 C^{-1})	Carrier mobility (cm^2 V^{-1} s^{-1})	Carrier concentration (10^{19} cm^{-3})	Electrical conductivity (10^4 S m^{-1})
BST	5.30	0.611	193	1.0	3.15
0.05%G/BST	4.83	0.639	197	0.98	3.07
0.10%G/BST	4.72	0.835	215	0.75	2.56
0.15%G/BST	4.60	0.784	173	0.80	2.20
0.20%G/BST	4.51	0.527	149	1.2	2.82

Fig. 3. SEI (a), BEI (b) image, and elemental mapping of C, Bi, Sb, and Te for 0.05%G/BST composites.

to the pores and volume effect caused by the low-density G. However, when the G content is higher than 0.10%, the charge transfer from G to BST becomes dominant, which leads to increased n. The positive values of α were indicative of p-type conduction behavior, which was consistent with the Hall measurements. With increasing the measuring temperature, α first increased and reached a maximum at 310–330 K and then decreased at higher temperatures. The increase of α was closely related to the reduced σ, while the reduction of α at higher temperatures was a consequence of intrinsic excitation. The α of the samples with $x \leq 0.15\%$ were increased compared with the G-free sample around room temperature, implying that the G particles had a positive effect on α. Normally, the relationship
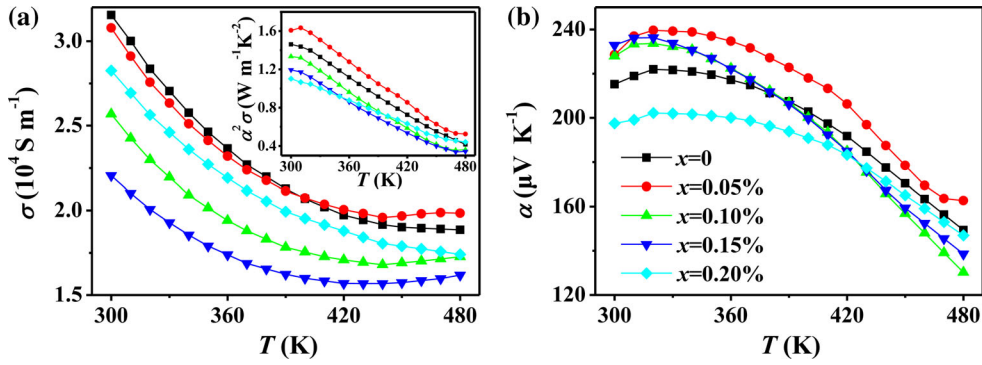
Fig. 4. Temperature dependences of (a) electrical conductivity and (b) Seebeck coefficient of xG/BST composites. Inset in (a) shows the temperature dependence of the power factor.
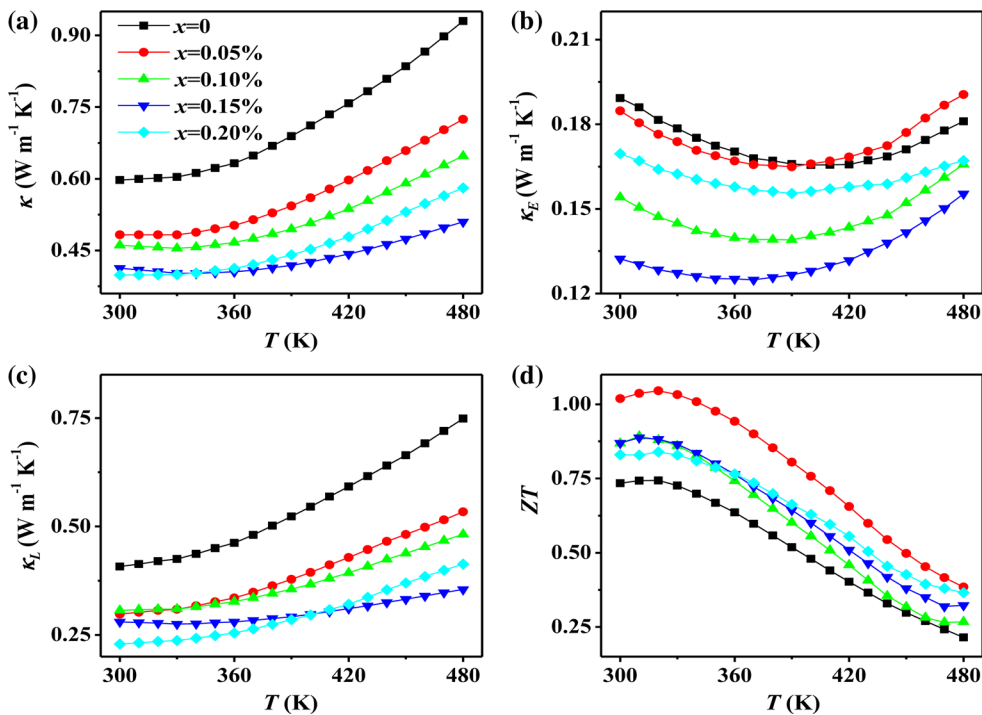

Fig. 5. Temperature dependences of (a) thermal conductivity, (b) carrier thermal conductivity, (c) lattice thermal conductivity, and (d) ZT of xG/BST composites.

between carrier concentration and Seebeck coefficient are inversely proportional. For a degenerated semiconductor and assuming a single parabolic band structure, it has,[10]

$$\alpha = \frac{8\pi^2 k_{\mathrm{B}}^2}{3eh^2} m^* T \left(\frac{\pi}{3n}\right)^{2/3} \quad (1)$$

Therefore, the improved Seebeck coefficient for the samples with $x < 0.15\%$ should be due to the decreased carrier concentration. The $\alpha^2\sigma$ of the sample with $x = 0.05\%$ increased slightly in the temperature range of 300–480 K as compared with the G-free sample, benefiting from the increased α.

The temperature dependences of thermal conductivity, carrier thermal conductivity, and lattice thermal conductivity of xG/BST composites are plotted in Fig. 5. The κ of the xG/BST composite TE materials increased with increasing the temperature in the range 300–480 K. The considerable increase at high temperatures was due to the bipolar effect in the intrinsic excitation region. The κ decreased as the x increased from 0% to 0.20%. The lowest κ was 0.40 W m^{-1} K^{-1} at 320 K for the sample with $x = 0.20\%$, showing a decrease of 33% as compared with the G-free BST matrix. Compared with other work, the thermal conductivities (0.4–0.6 W m^{-1} K^{-1}) of our cold-pressed samples are

much lower than those of the higher-density samples synthesized by the spark plasma sintering process (over 1.0 W m^{-1} K^{-1}).[25] κ_L was significantly reduced, which should be attributed to the enhanced phonon scattering induced by the pores and G particles. In fact, the rather low density should be largely responsible for the extremely low κ_L. The change trend in κ_E as the temperature increases was attributed to the contribution of the temperature according to the temperature of the σ. Figure 5d shows the ZT values of the xG/BST composites. As the temperature increased in the range of 300–480 K, ZT first increased and then decreased. The largest ZT reached 1.05 at 320 K for the composite with $x = 0.05\%$, which is increased by 35% as compared with that of the G-free BST matrix. Note that the G/BST composites showed high ZT values comparable with those of commercialized zone-melting ingots. The property measurements clearly indicated that optimizing the content of the G particles could significantly increase the TE performance of the BST due to the remarkable decrease in κ and slight increase in $\alpha^2\sigma$.

CONCLUSIONS

A series of xG/BST ($x = 0\%$, 0.05%, 0.10%, 0.15%, and 0.20%) composite TE materials were prepared by the combination of powder metallurgy, cold-pressing, and annealing methods. XRD analysis showed that all the composites were composed of BST phase with no preferred orientation. Charge transport measurements demonstrated that the carrier concentration first decreased due to the decreased density, then increased due to the addition of conductive G. TE transport measurements indicated that optimizing the doping content of G particles could enhance $\alpha^2\sigma$ due to the slight increases in α. The maximal $\alpha^2\sigma$ value reached 1.63 mW m^{-1} K^{-2} at 310 K for the sample with $x = 0.05\%$. κ_L was significantly reduced, by 33%, because of enhanced phonon scattering induced by the pores and G particles. The largest ZT for the composites with $x = 0.05\%$ reached 1.05 at 320 K, which is increased by 35% as compared with G-free BST materials. This work provided a simple and cost-effective approach to achieve non-textured Bi$_2$Te$_3$-based TE materials with comparable TE performance.

ACKNOWLEDGEMENTS

REFERENCES

1. L.E. Bell, *Science* 321, 1457 (2008).
2. T.C. Harman, P.J. Taylor, and M.P. Walsh, *Science* 297, 2229 (2002).
3. A.I. Hochbaum, R.K. Chen, R.D. Delgado, W.J. Liang, E.C. Garnett, and M. Najarian, *Nature* 451, 163 (2008).
4. B.C. Sales, D. Mandrus, and R.K. Williams, *Science* 272, 1325 (1996).
5. W.Y. Zhao, P. Wei, Q.J. Zhang, C.L. Dong, L.S. Liu, and X.F. Tang, *J. Am. Chem. Soc.* 131, 3713 (2009).
6. P. Wei, W.Y. Zhao, C.L. Dong, X. Yang, J. Yu, and Q.J. Zhang, *Acta Mater.* 59, 3244 (2011).
7. L.D. Zhao, S.H. Lo, Y.S. Zhang, H. Sun, G.J. Tan, C. Uher, C. Wolverton, V.P. Dravid, and M.G. Kanatzidis, *Nature* 508, 373 (2014).
8. M. Christensen, S. Johnsen, and B.B. Iversen, *Dalton Trans.* 39, 978 (2010).
9. H.L. Liu, X. Shi, F.F. Xu, L.L. Zhang, W.Q. Zhang, L.D. Chen, Q. Li, C. Uher, T. Day, and G.J. Snyder, *Nat. Mater.* 11, 422 (2012).
10. G.J. Snyder and E.S. Toberer, *Nat. Mater.* 7, 50 (2008).
11. J.P. Heremans, V. Jovovic, E.S. Toberer, A. Saramat, K. Kurosaki, A. Charoenphakdee, S. Yamanaka, and G.J. Snyder, *Science* 321, 554 (2008).
12. M.S. Dresselhaus, G. Chen, M.Y. Tang, R.C. Yang, H. Lee, D.Z. Wang, Z.F. Ren, J.-P. Fleurial, and P. Gogna, *Adv. Mater.* 19, 1043 (2007).
13. B. Poudel, Q. Hao, Y. Ma, Y.C. Lan, A. Minnich, B. Yu, X. Yan, D. Wang, A. Muto, D. Vashaee, X.Y. Chen, J. Liu, M.S. Dresselhaus, G. Chen, and Z.F. Ren, *Science* 320, 634 (2008).
14. G.Q. Zhang, Q.X. Yu, W. Wang, and X.G. Li, *Adv. Mater.* 22, 1959 (2010).
15. J.F. Li, W.S. Liu, L.D. Zhao, and M. Zhou, *NPG Asia Mater.* 2, 152 (2010).
16. X. Yan, B. Poudel, Y. Ma, W.S. Liu, G. Joshi, H. Wang, Y.C. Lan, D.Z. Wang, G. Chen, and Z.F. Ren, *Nano Lett.* 10, 3373 (2010).
17. W.J. Xie, J. He, H.J. Kang, X.F. Tang, S. Zhu, M. Laver, S.Y. Wang, J.R.D. Copley, C.M. Brown, Q.J. Zhang, and T.M. Tritt, *Nano Lett.* 10, 3283 (2010).
18. A.P. Yu, P. Ramesh, X.B. Sun, E. Bekyarova, M.E. Itkis, and R.C. Haddon, *Adv. Mater.* 20, 4740 (2008).
19. Y.W. Zhang, X.P. Jia, H. Sun, B.R. Sun, B.W. Liu, H.Q. Liu, L.J. Kong, and H.A. Ma, *J Materiomics* 2, 316 (2016).
20. W.B. Zhou, Q.X. Fan, Q. Zhang, L. Cai, K.W. Li, X.G. Gu, F. Yang, N. Zhang, Y.C. Wang, H.P. Liu, W.Y. Zhou, and S.S. Xie, *Nat. Commun.* 8, 14886 (2017).
21. J. Dong, W. Liu, H. Li, X. Su, X. Tang, and C. Uher, *J. Mater. Chem. A* 1, 12503 (2013).
22. B. Feng, J. Xie, G. Cao, T. Zhu, and X. Zhao, *J. Mater. Chem. A* 1, 13111 (2013).
23. T. Zhang, J. Jiang, Y. Xiao, Y. Zhai, S. Yang, and G. Xu, *ACS Appl. Mater. Interfaces.* 5, 3071 (2013).
24. D. Suh, S. Lee, H. Mun, S.H. Park, K.H. Lee, S.W. Kim, J.Y. Choi, and S. Bailk, *Nano Energy* 13, 67 (2015).
25. D.W. Xie, G.Q. Liu, X.J. Tan, J. Jiang, J.T. Xu, Z. Liu, and H.Z. Shao, *Energies* 9, 4 (2016).